Materials Advances

ROYAL SOCIETY OF CHEMISTRY

PAPER

View Article Online
View Journal | View Issue



Cite this: *Mater. Adv.*, 2026, 7, 5833

# A multifunctional GaMOF–$Cu_2O$-integrated GelMA hydrogel for synergistic antibacterial activity and tissue regeneration

Hai Zhu, Yue Gao, Yu Sun, Huan Liu, Xiaoming Tang* and Feng Ji*

Received 22nd December 2025,
Accepted 23rd April 2026

DOI: 10.1039/d5ma01501d

rsc.li/materials-advances

The rising threat of multidrug-resistant (MDR) bacterial infections and resilient biofilms in bone and soft tissue, exacerbated by antibiotic misuse, demands the development of novel non-antibiotic therapeutics that combine effective bactericidal activity with tissue-regenerative functions. To address this challenge, we developed a multifunctional gelatin methacryloyl (GelMA) hydrogel platform loaded with a gallium-based metal–organic framework and copper(I) oxide nanocomposite (GaMOF–$Cu_2O$). This system leverages a synergistic antibacterial mechanism: $Ga^{3+}$ ions disrupt critical iron metabolism by mimicking $Fe^{3+}$, while $Cu^{+}$ ions catalyze the generation of reactive oxygen species (ROS) to inflict oxidative damage. Together, this dual action potently eradicates bacteria and inhibits biofilm formation. Simultaneously, the GelMA hydrogel matrix ensures localized and sustained release of the therapeutic agents and provides a bioactive, three-dimensional scaffold that facilitates cell migration and angiogenesis, thereby supporting tissue repair. Our findings demonstrate that the GaMOF–$Cu_2O$/GelMA hydrogel is a highly promising and integrative strategy for combating refractory MDR and biofilm-associated infections while promoting tissue regeneration, offering a potent alternative to conventional antibiotic therapies.



## 1. Introduction

Bone and soft tissue infections, particularly those caused by multidrug-resistant (MDR) bacteria such as *Staphylococcus aureus* and *Pseudomonas aeruginosa*, represent a severe global health challenge.[1–4] The widespread misuse of antibiotics has accelerated the emergence of antibiotic-resistant pathogens, significantly compromising the efficacy of conventional antibacterial therapies and increasing the risk of chronic infection and treatment failure.[5–8] In clinical practice, persistent bacterial infections within deep tissues or on implant surfaces often form biofilms that act as protective barriers against antibiotics and immune clearance, making the eradication of pathogens particularly difficult. Therefore, developing novel, non-antibiotic-dependent antibacterial strategies that can efficiently eliminate bacteria and simultaneously promote tissue regeneration is of critical importance for addressing refractory bone and soft tissue infections.

Gallium (Ga), a group IIIA metal, has attracted significant attention as a promising antibacterial agent due to its unique ability to mimic ferric ions ($Fe^{3+}$) but remain redox-inactive.[9–13] This enables gallium to disrupt bacterial iron metabolism and impair essential enzymatic functions that rely on iron cofactors, leading to inhibition of DNA synthesis, suppression of oxidative stress defense systems, and eventual bacterial death. Such a "Trojan horse" mechanism allows $Ga^{3+}$ to infiltrate bacterial cells by substituting $Fe^{3+}$ in key metabolic enzymes, thereby disturbing intracellular redox balance and sensitizing bacteria to oxidative stress. Metal–organic frameworks (MOFs), featuring a highly porous crystalline structure composed of metal nodes and organic ligands, provide an ideal platform for the controlled release of $Ga^{3+}$ and for the incorporation of other therapeutic components.[14–18] Gallium-based MOFs (GaMOFs) thus combine the chemical versatility of MOFs with the intrinsic antibacterial activity of Ga ions, exhibiting superior antibacterial performance, tunable degradation behavior, and favorable biocompatibility.[19–21]

To further enhance bactericidal efficiency, copper(I) oxide ($Cu_2O$) can be incorporated into GaMOFs to create a dual-functional antibacterial system. $Cu_2O$ possesses intrinsic photocatalytic and redox properties that can catalyze the generation of reactive oxygen species (ROS), such as hydroxyl radicals ($^{\bullet}OH$) and superoxide anions ($O_2^{\bullet-}$), under physiological or light-stimulated conditions.[22–25] The synergistic interaction between $Ga^{3+}$ and $Cu^{+}$ offers a dual mechanism of antibacterial action: disruption of bacterial metabolic processes *via* Ga-mediated iron substitution, and oxidative damage through Cu-induced ROS production.[26–28] This combined effect can effectively destroy bacterial cell membranes, inhibit biofilm

*Department of Orthopedic Surgery, The Affiliated Huaian No. 1 People's Hospital of Nanjing Medical University, Huaian, China*

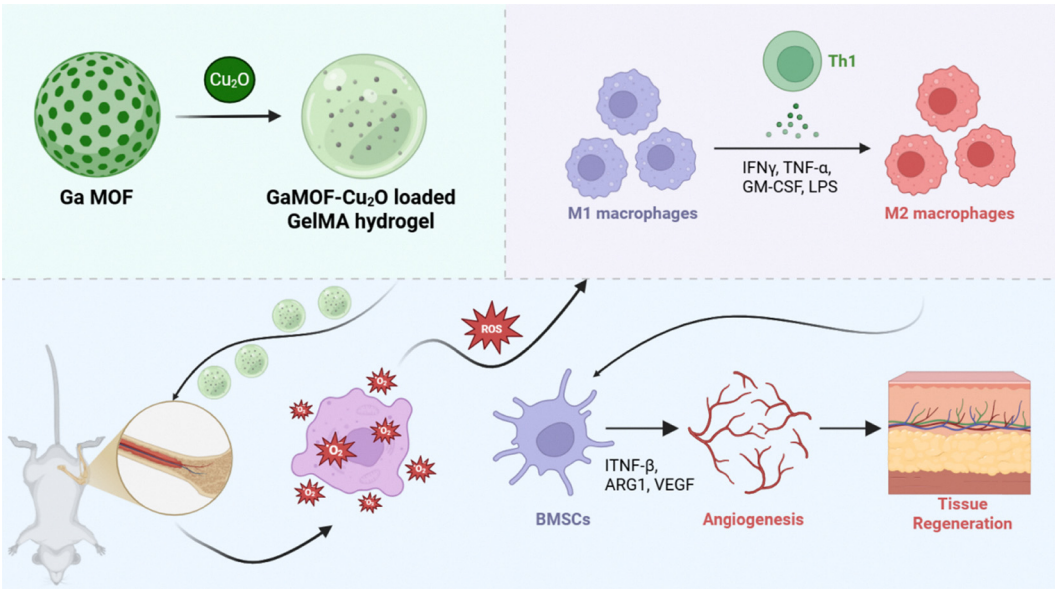


Scheme 1 Schematic of the mechanism of the GelMA@GaCu induced infected tissue regeneration.

formation, and overcome intracellular bacterial persistence—major factors contributing to chronic and recurrent infections.

For effective local administration and tissue repair, embedding the GaMOF–$Cu_2O$ nanocomposite within a gelatin methacryloyl (GelMA) hydrogel matrix offers a versatile and clinically translatable approach. GelMA hydrogels possess excellent biocompatibility, biodegradability, and tunable mechanical properties, making them suitable for wound dressing and tissue engineering applications.[29–34] Acting as a three-dimensional (3D) scaffold, GelMA not only enables localized and sustained release of the nanocomposite but also provides a moist, bioactive environment conducive to angiogenesis, cell migration, and new tissue formation. The integration of GaMOF–$Cu_2O$ with GelMA thus enables a multifunctional therapeutic platform that unites infection control with regenerative support.

In this study, we designed and fabricated a GaMOF–$Cu_2O$-loaded GelMA hydrogel with synergistic antibacterial and tissue-healing capabilities for the treatment of bone and soft tissue infections. The combination of gallium-mediated metabolic disruption, copper-induced oxidative stress, and hydrogel-assisted regeneration is expected to achieve efficient bacterial eradication, suppression of local inflammation, and acceleration of tissue repair. This work proposes a novel, multi-mechanistic antibacterial system that holds great potential as a next-generation therapeutic strategy against antibiotic-resistant and biofilm-associated infections in orthopedic and soft tissue settings (Scheme 1).

## 2. Results and discussion

### 2.1 Synthesis and characterization of GelMA@Ga and GelMA@GaCu

The morphology and physicochemical characteristics of GelMA@GaCu were systematically examined to validate the successful construction of the nanocomposite. As shown in Fig. 1a, TEM imaging revealed that GelMA@GaCu exhibited a compact and irregularly aggregated architecture with nanoscale sub-domains, indicating that the incorporation of Ga/Cu components did not compromise the intrinsic structural integrity of the hydrogel-based framework. Higher-magnification images further demonstrated the presence of densely packed nanoregions and rough surface textures, suggesting a heterogeneous internal structure conducive to ion release.

The hydrodynamic size distribution obtained by DLS (Fig. 1b) showed a single, narrow peak centered around ~200 nm, confirming the formation of relatively uniform nanoparticles following Ga/Cu integration. This size range is favorable for cellular interaction and ensures adequate dispersion stability in aqueous environments.

To evaluate the release characteristics of Ga ions from the composite, cumulative release profiles were monitored under mildly acidic (pH 6.0) and physiological (pH 7.4) conditions (Fig. 1c). A markedly accelerated release was observed at pH 6.0, where Ga liberation increased rapidly during the first 24 h and gradually plateaued thereafter. In contrast, release at pH 7.4 proceeded more slowly, reflecting the pH-responsive degradation behavior of the material and its potential for targeted ion delivery in infection-associated acidic microenvironments.

The surface charge properties of GaMOF and GaCuMOF were further assessed through zeta potential measurements (Fig. 1d). Compared with GaMOF, the GaCu-modified structure displayed a less negative surface potential, implying that Cu incorporation altered the interfacial charge distribution and improved the colloidal stability of the resulting nanocomposite. The shift in zeta potential also indicates enhanced interaction capability with bacterial membranes and biological interfaces. The ROS generation capacity of different hydrogel formulations was evaluated using a fluorescence assay. As shown in Fig. 1e, the GelMA@GaCu group exhibited significantly higher ROS levels compared with the Control, GelMA, and GelMA@Ga

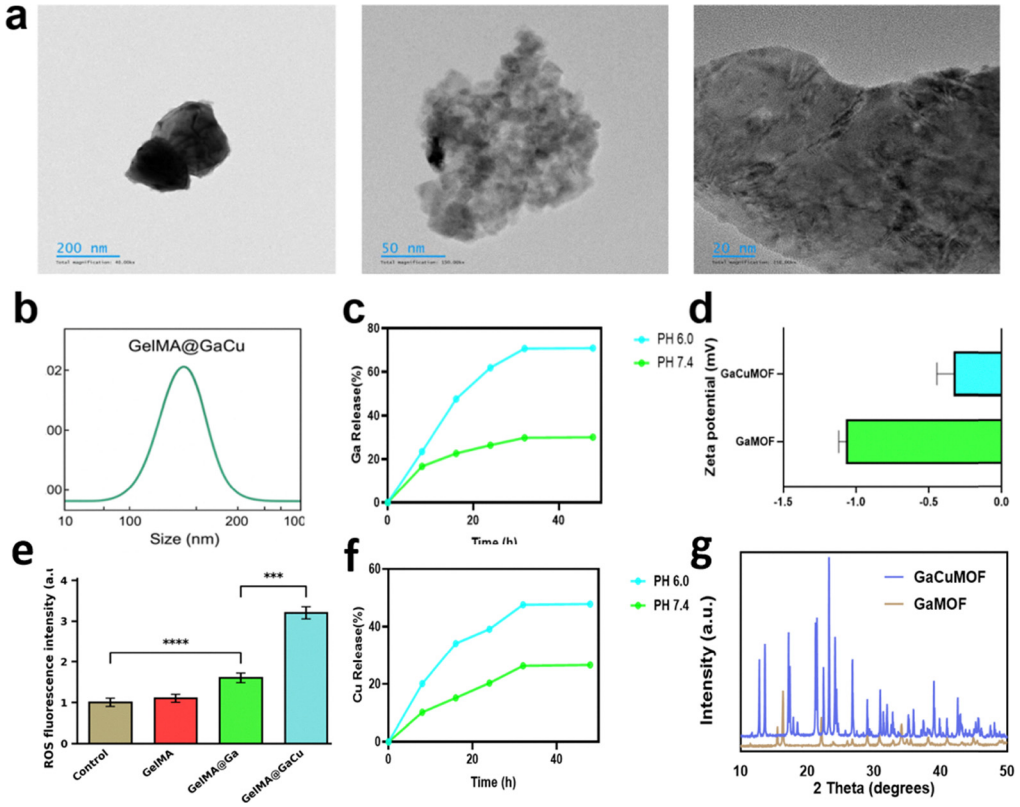


Fig. 1 Synthesis and Characterization of GelMA@Ga and GelMA@GaCu. (a) TEM images of GelMA@GaCu showing its aggregated nanoscale structure and heterogeneous internal morphology at different magnifications. (b) Hydrodynamic size distribution of GelMA@GaCu determined by DLS, exhibiting a unimodal peak centered around ~200 nm. (c) Cumulative Ga ion release profiles under pH 6.0 and pH 7.4 conditions, demonstrating enhanced pH-responsive release in acidic environments. (d) Zeta potential measurements of GaMOF and GaCuMOF, indicating surface charge variation following Cu incorporation. (e) Quantitative analysis of ROS generation in different groups. Data are presented as mean ± SD ($n$ = 3). ***$p < 0.001$, ****$p < 0.0001$. (f) Cumulative Cu ion release profiles under pH 6.0 and pH 7.4 conditions. (g) XRD patterns of GaMOF and GaCuMOF.

groups, indicating that the incorporation of Cu markedly enhanced oxidative stress generation. This elevated ROS production is expected to contribute to the improved antibacterial activity of the composite hydrogel. The Cu ion release behavior was further investigated under physiological (pH 7.4) and mildly acidic (pH 6.0) conditions (Fig. 1f). The results showed a sustained release profile, with a faster release rate under acidic conditions, suggesting that the material may respond to the infection-associated acidic microenvironment. Additionally, XRD analysis revealed that the characteristic diffraction peaks of GaCuMOF largely overlapped with those of GaMOF (Fig. 1g), indicating that the introduction of Cu species did not significantly alter the crystalline framework of the MOF structure.

Collectively, these results confirm that GelMA@GaCu possesses well-defined nanoscale morphology, favorable particle size, pH-responsive Ga release, and modified surface charge—features that jointly contribute to its antibacterial and therapeutic performance.

### 2.2 The *in vitro* antibacterial properties of GelMA@Ga and GelMA@GaCu

To elucidate the antibacterial capacity of the Ga/Cu–integrated hydrogel system, the bactericidal effects of four formulations—control, GelMA, GelMA@Ga, and GelMA@GaCu—were systematically examined using *Staphylococcus aureus* as a representative Gram-positive pathogen. Colony-counting assays revealed a stepwise enhancement in antimicrobial efficacy following metal incorporation. As shown in Fig. 2a, GelMA alone exerted negligible influence on bacterial proliferation, whereas GelMA@Ga substantially reduced the number of viable colonies. Notably, the dual-metal hydrogel GelMA@GaCu achieved the most prominent bactericidal activity, exhibiting an almost complete eradication of surviving bacteria. This trend was further corroborated by quantitative plating data (Fig. 2c), which demonstrated a significant decline in colony-forming units, underscoring the synergistic contribution of Ga and Cu to microbial suppression.

Given the clinical relevance of biofilm-associated infections, we next assessed the capacity of the hydrogels to inhibit biofilm formation. Crystal violet staining (Fig. 2b) revealed that biofilms in the control and GelMA groups remained dense and structurally intact. In contrast, GelMA@Ga and especially GelMA@GaCu produced a marked reduction in biofilm biomass, as reflected by the substantially decreased OD values (Fig. 2d). The declining trend in residual biofilm mass was consistent with overall bacterial survival (Fig. 2e), collectively indicating that dual-metal doping significantly impairs both planktonic and biofilm-embedded bacteria.

To further visualize structural alterations induced by the hydrogels, scanning electron microscopy (SEM) was performed.

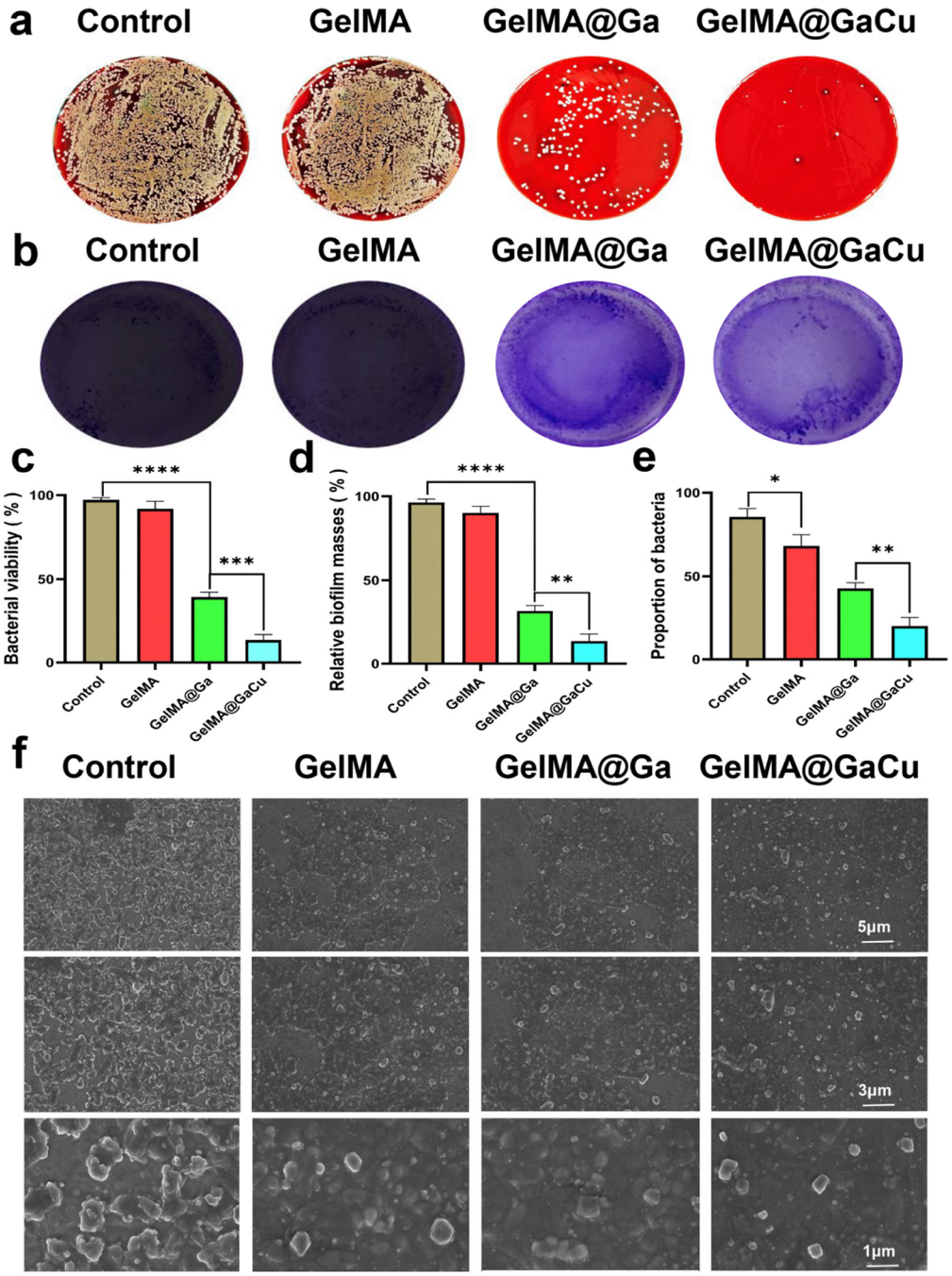


Fig. 2 *In vitro* antibacterial performance of GelMA@Ga and GelMA@GaCu. (a) Representative blood agar plates showing colony-forming units (CFUs) of *S. aureus* after treatment with Control, GelMA, GelMA@Ga, and GelMA@GaCu hydrogels. (b) Photographs of crystal violet–stained *S. aureus* biofilms formed after exposure to different hydrogel formulations. (c) Quantitative bacterial viability measured after each treatment. (d) Relative biofilm biomass remaining on the substrate following different hydrogel treatments. (e) Quantitative analysis of the proportion of surviving bacteria in each group. (f) Scanning electron microscopy (SEM) images showing the microstructural morphology of *S. aureus* biofilms after treatment, highlighting the progressive disruption of cell integrity from GelMA to GelMA@Ga and GelMA@GaCu. Scale bars: 5 μm, 3 μm, 1 μm. Data are shown as mean ± s.d. ($n$ = 3). Significance levels: *$p < 0.1$, **$p < 0.01$, ***$p < 0.001$, ****$p < 0.0001$.

As shown in Fig. 2f, untreated bacteria formed compact microcolonies with smooth cell surfaces. GelMA@Ga treatment caused modest morphological perturbation, including partial membrane roughening and loss of turgor. Strikingly, GelMA@GaCu induced extensive structural collapse, surface wrinkling, and membrane rupture, demonstrating severe bacterial damage consistent with its enhanced antimicrobial performance. These observations suggest that Ga and Cu jointly interfere with bacterial metabolic homeostasis, membrane integrity, and biofilm architecture.

Taken together, the combined quantitative and morphological analyses indicate that GelMA@GaCu exhibits potent

bactericidal and antibiofilm activities. The dual-metal hydrogel not only suppresses bacterial proliferation but also disrupts established biofilm structures, highlighting its strong potential for addressing persistent and biomaterial-related infections.

### 2.3 *In vitro* immunomodulatory effects of GelMA@Ga and GelMA@GaCu on macrophage polarization.

Effective immune regulation is indispensable for orchestrating tissue regeneration during the resolution of infection.[35] Considering that thermal interventions may inadvertently impair soft tissues and hinder repair, recent studies have emphasized steering macrophage phenotypes as a therapeutic avenue for enhancing healing outcomes. In this context, we evaluated whether GelMA-based hydrogels containing Ga and Cu could modulate macrophage polarization and promote a pro-regenerative immune milieu.

RAW264.7 macrophages were employed to assess the immunoregulatory capacity of the different hydrogel formulations.[36–39] As illustrated in Fig. 3a, immunofluorescence staining revealed a marked decline in CCR7 expression (M1-associated marker, red) and a concurrent elevation in CD206 expression (M2-associated marker, green) when cells were treated with GelMA@Ga and, more prominently, GelMA@GaCu. Quantitative analysis of fluorescence intensity (Fig. 3b–c) confirmed these trends, demonstrating a significant suppression of pro-inflammatory M1 polarization alongside an enhancement of M2 phenotype induction.

Cytokine secretion profiles further corroborated this shift. ELISA assays (Fig. 3d–e) showed that GelMA@GaCu significantly reduced the levels of IFN-γ—a key inflammatory cytokine—while simultaneously elevating anti-inflammatory IL-10, reflecting a transition toward a reparative immune state. In parallel, gene expression analyses of osteogenic-associated markers, including BMP2 and OCN (Fig. 3f–g), revealed substantial upregulation in the GelMA@GaCu group, suggesting that the immunomodulatory shift may secondarily contribute to a microenvironment favorable for tissue regeneration.

Collectively, these results demonstrate that Ga/Cu co-doped hydrogels effectively facilitate macrophage polarization toward the M2 phenotype, attenuate inflammatory cytokine production, and enhance regenerative signaling pathways, thereby underscoring their potential in supporting post-infection tissue repair.

### 2.4 *In vitro* pro-regenerative effects of GelMA@Ga and GelMA@GaCu

To further clarify the effects of the GelMA-based hydrogels on BMSC-mediated tissue repair, we performed a series of *in vitro* assays evaluating cytoskeletal organization and osteogenic differentiation (Fig. 4a–d). As shown in Fig. a, confocal imaging revealed notable differences in BMSC morphology among the four treatment groups (control, GelMA, GelMA@Ga, and GelMA@GaCu). While cells in the control and GelMA groups exhibited relatively limited spreading, both GelMA@Ga and GelMA@GaCu promoted marked cytoskeletal expansion, with the GelMA@GaCu group displaying the most pronounced actin fiber organization. This enhanced spreading morphology suggests increased cellular activation and a pro-osteogenic cytoskeletal state.

We next examined the transcriptional levels of osteogenesis-related genes. As presented in Fig. 4b, β-catenin expression showed a significant upregulation in the GelMA@GaCu group compared to all other treatments, whereas GelMA alone had no observable effect relative to the control. A similar trend was observed for Col1 expression (Fig. 4c): GelMA@Ga induced a moderate increase, while GelMA@GaCu resulted in the highest expression level, indicating synergistic enhancement of extracellular matrix production.

Consistent with gene expression findings, alkaline phosphatase (ALP) activity—a hallmark of early osteogenic differentiation—was substantially elevated in the GelMA@GaCu group (Fig. 4d). In contrast, ALP activity in the control and GelMA groups remained at baseline levels, with GelMA@Ga exhibiting a moderate but notable increase. These results collectively demonstrate that the incorporation of Ga and the dual Ga–Cu modification significantly improves the osteogenic responsiveness of BMSCs, with GelMA@GaCu achieving the strongest pro-osteogenic effect among the tested materials. To further evaluate the biosafety of the hydrogel formulations, a CCK-8 assay was performed to assess cell viability after incubation with different groups. As shown in Fig. S3, all hydrogel groups maintained high cell viability, and no significant difference was observed among the Control, GelMA, GelMA@Ga, and GelMA@GaCu groups. These results indicate that the incorporation of Ga and Cu did not induce obvious cytotoxicity under the tested conditions, confirming the favorable cytocompatibility and biosafety of the hydrogel system for further biomedical applications.

### 2.5 *In vitro* pro-regenerative effects of GelMA@Ga and GelMA@GaCu

The *in vivo* therapeutic performance of the GelMA-based hydrogels was examined using a bacteria-infected wound model following the experimental schedule illustrated in Fig. 5a. Histological evaluation provided clear evidence of differential wound responses among the treatment groups (Fig. 5b and Fig. S1). In both the control and GelMA groups, H&E staining showed persistent inflammatory cell infiltration and incomplete re-epithelialization, accompanied by loosely organized granulation tissue. In contrast, the GelMA@Ga group exhibited a moderate reduction in inflammatory burden and partial restoration of tissue architecture. The most substantial improvement was observed in the GelMA@GaCu group, where the dermal structure appeared more integrated, inflammatory infiltration was markedly diminished, and new tissue organization was more consistent with progressing wound resolution.

Masson trichrome staining further delineated collagen deposition patterns across groups. As shown in Fig. 5c, the GelMA@GaCu-treated wounds demonstrated significantly higher collagen content and more mature fiber alignment relative to the control and GelMA groups, indicating a more advanced state of matrix remodeling. Quantitative analysis

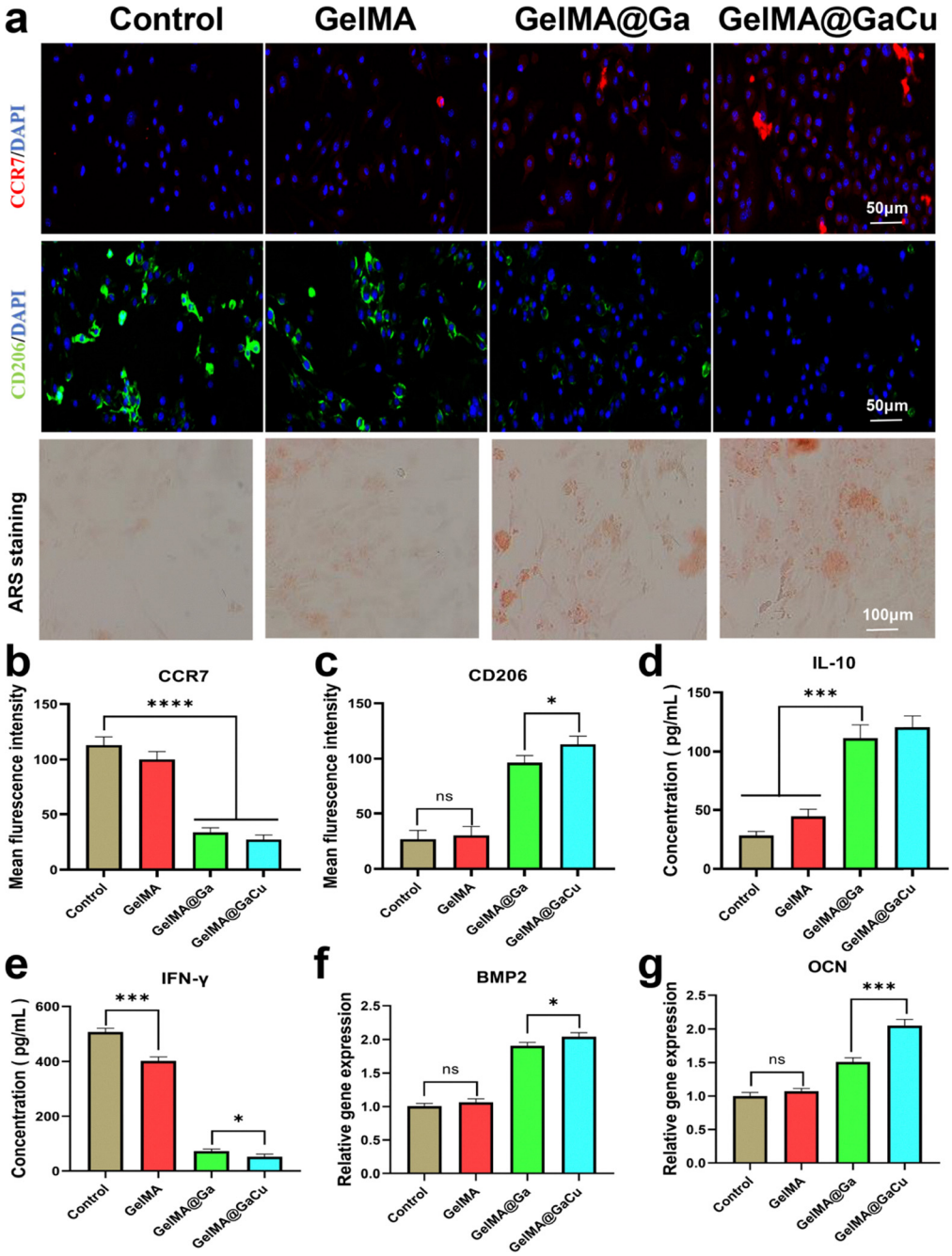


Fig. 3 *In vitro* immunomodulatory effects of GelMA@Ga and GelMA@GaCu on macrophage polarization. (a) Immunofluorescence staining of RAW264.7 cells after different treatments, showing CCR7 (M1 marker, red) and CD206 (M2 marker, green) expression. Nuclei were counterstained with DAPI (blue). (b) and (c) Quantitative analysis of fluorescence intensities corresponding to CCR7 and CD206, respectively. (d) and (e) ELISA results demonstrating changes in inflammatory cytokine secretion, including IFN-γ and IL-10, across the treatment groups. (f) and (g) qRT-PCR analysis of osteogenic-related genes BMP2 and OCN, indicating the pro-regenerative signaling induced by the hydrogels. Data are presented as mean ± s.d. ($n$ = 3). Statistical significance: *$p < 0.1$, **$p < 0.01$, ***$p < 0.001$, ****$p < 0.0001$; ns, not significant.

confirmed the superiority of the GelMA@GaCu treatment, with the highest collagen volume fraction among all groups.

*In vivo* antibacterial efficacy was assessed through bacterial enumeration on Day 21. The GelMA@Ga and GelMA@GaCu hydrogels both reduced bacterial load compared with the untreated wounds, with GelMA@GaCu achieving the most pronounced reduction in CFU counts (Fig. 5d). Corresponding bacterial viability analysis (Fig. 5e) corroborated these findings, showing the lowest proportion of viable bacteria in the GelMA@GaCu group.

Together, these results indicate that incorporating Ga and Cu into the GelMA matrix produces a synergistic effect, enabling more effective bacterial suppression while concurrently promoting collagen deposition and inflammation

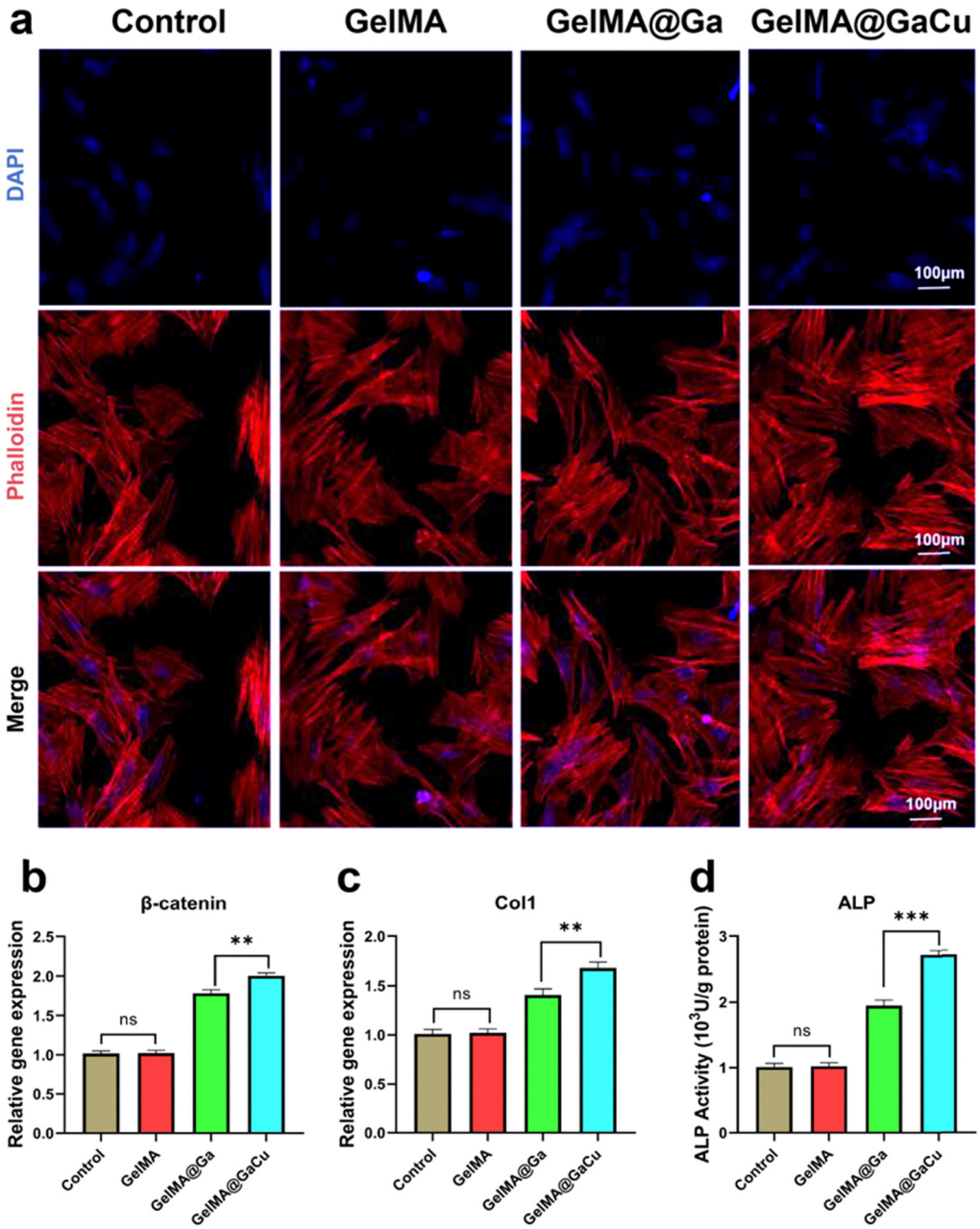


Fig. 4 *In vitro* pro-regenerative effects of GelMA@Ga and GelMA@GaCu. (a) Fluorescence images of bone marrow mesenchymal stem cells (BMSCs) cultured on different hydrogels, stained with DAPI (nuclei, blue) and phalloidin (F-actin, red). The cytoskeletal morphology demonstrates progressively enhanced cell spreading and filament organization from GelMA to GelMA@Ga and GelMA@GaCu. Scale bar: 100 μm. (b) Relative mRNA expression levels of β-catenin in BMSCs after incubation with the hydrogels, showing activation of Wnt-related signaling pathways in Ga/Cu-containing groups. (c) Gene expression of Col1 (collagen type I), indicating enhanced extracellular matrix synthesis stimulated by the hydrogel formulations. (d) Quantitative alkaline phosphatase (ALP) activity, demonstrating significantly increased early osteogenic differentiation in the GelMA@GaCu group. Data are presented as mean ± s.d. ($n$ = 3). Statistical significance: $^{**}p < 0.01$, $^{***}p < 0.001$; ns, not significant.

resolution. This dual action contributes to a more favorable wound healing trajectory in the infected wound model.

### 2.6 Transcriptomic remodeling of BMSCs induced by GelMA@GaCu

To further elucidate the molecular mechanisms underlying the pro-regenerative effects of GelMA@GaCu on bone marrow mesenchymal stem cells (BMSCs), we conducted transcriptomic profiling to characterize the global gene expression changes induced by the material. As shown in Fig. 6a, hierarchical clustering revealed a distinct transcriptional signature between GelMA@GaCu-treated cells and the untreated control group. A series of genes associated with extracellular matrix remodeling (*e.g.*, COL1A1, COL1A2), cell adhesion, and

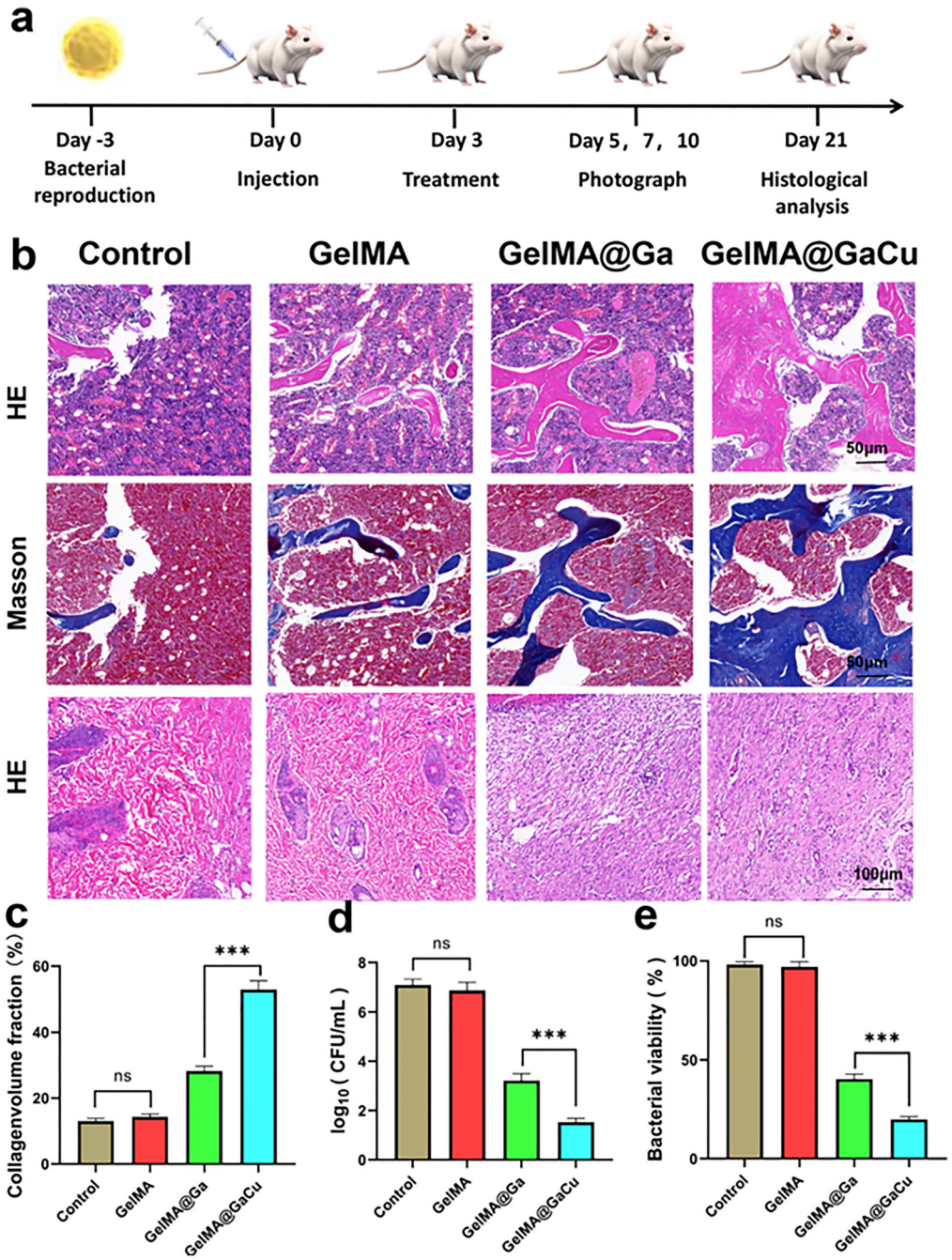


Fig. 5 *In vivo* evaluation of infected wound healing following treatment with GelMA@Ga and GelMA@GaCu. (a) Schematic timeline of the *in vivo* experimental procedure, including bacterial infection, hydrogel administration, serial monitoring, and tissue collection from Day −3 to Day 21. (b) Representative H&E and Masson staining images of wound tissues harvested on Day 21 in the control, GelMA, GelMA@Ga, and GelMA@GaCu groups. The GelMA@GaCu-treated wounds exhibited reduced inflammatory infiltration and more organized tissue architecture, along with enhanced collagen deposition. Scale bar: 100 μm. (c) Quantitative analysis of collagen volume fraction based on Masson staining, demonstrating significantly increased collagen regeneration in the GelMA@GaCu group compared with other treatment groups. (d) Bacterial colony-forming unit (CFU) counts from wound tissues on Day 21, showing reduced bacterial load in GelMA@Ga and GelMA@GaCu groups, with GelMA@GaCu achieving the greatest antibacterial effect. (e) Bacterial viability analysis from wound homogenates, indicating the lowest proportion of viable bacteria in the GelMA@GaCu group. Data are presented as mean ± SD. Statistical significance: $p < 0.05$, $p < 0.01$, $p < 0.001$.

osteogenic commitment exhibited marked upregulation, whereas several inflammation- or stress-related genes were significantly downregulated.

The volcano plot (Fig. 6b) further highlighted the extent of transcriptomic reprogramming. A substantial number of genes were differentially expressed upon GelMA@GaCu stimulation,

with key upregulated genes including SPP1, ZYX, and GXYLT1—all of which participate in matrix deposition, cytoskeletal organization, and osteogenic differentiation.[40,41] Conversely, downregulated genes such as SLC1A2 and CCL11 have been previously associated with inhibitory or inflammatory pathways, suggesting that GelMA@GaCu may attenuate negative regulators of regeneration while promoting osteo-active transcriptional programs.

Gene ontology (GO) enrichment analysis (Fig. 6c) provided further insight into these functional shifts. Upregulated genes were strongly enriched in biological processes related to extracellular matrix organization, cytoskeleton regulation, ion channel activity, and transporter complex assembly—pathways that collectively support enhanced cellular adhesion, morphological maturation, and osteogenic signaling. Enrichment in structural components such as intermediate filaments, microvilli, and

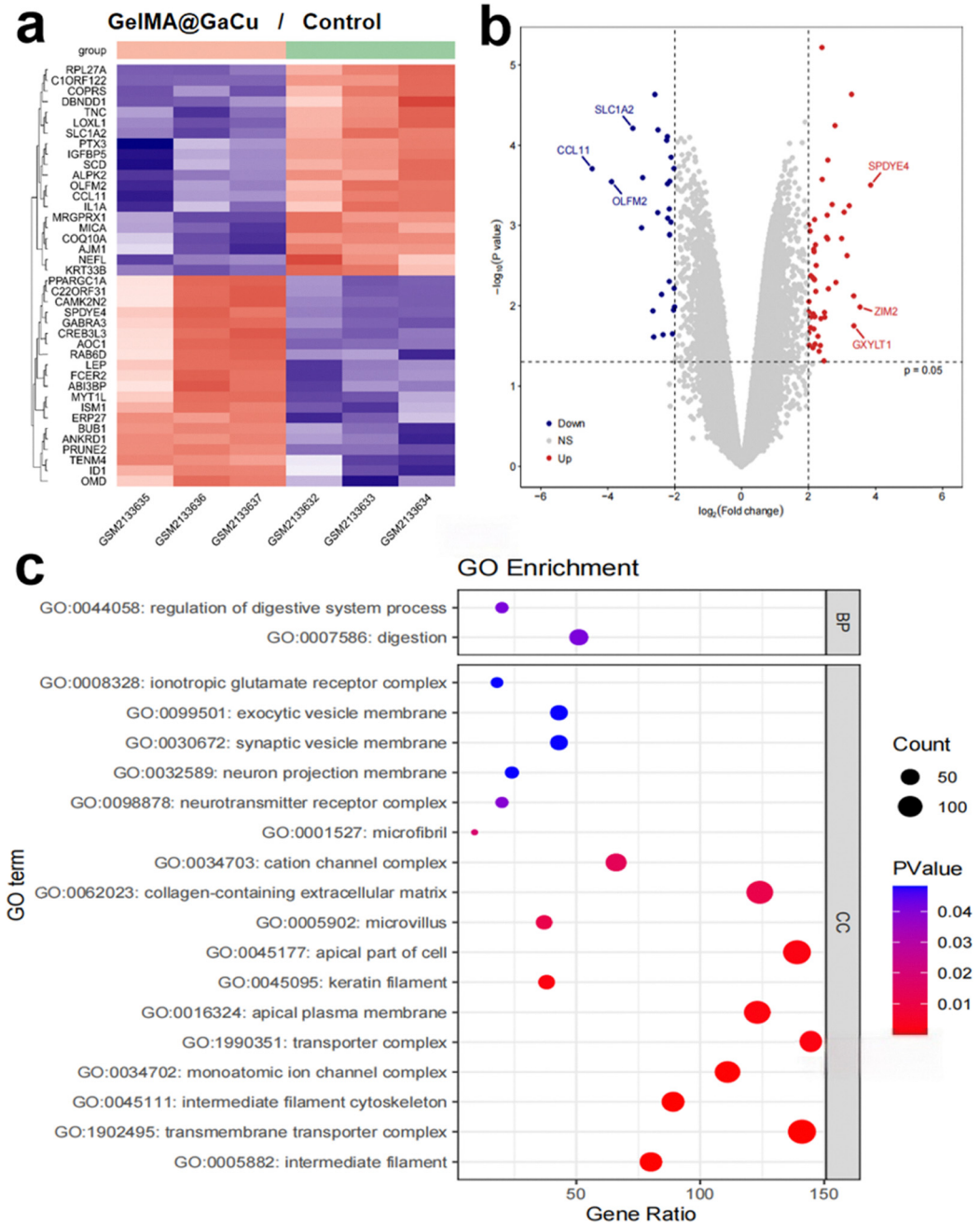


Fig. 6 Transcriptomic remodeling of BMSCs induced by GelMA@GaCu. (a) Heatmap of differentially expressed genes showing distinct transcriptional clustering between GelMA@GaCu-treated BMSCs and control groups. (b) Volcano plot illustrating significantly upregulated (red) and downregulated (blue) genes following GelMA@GaCu stimulation, with representative genes annotated. (c) Gene Ontology (GO) enrichment analysis of differentially expressed genes, highlighting biological processes (BP) and cellular components (CC) related to extracellular matrix organization, cytoskeletal regulation, ion channel complexes, and transporter complexes.

collagen-containing ECM suggests that GelMA@GaCu may promote the establishment of a mechanically supportive and functionally active cellular niche conducive to bone regeneration.

Together, these findings indicate that GelMA@GaCu exerts a multifaceted regulatory influence on BMSCs, reshaping their transcriptional landscape toward a pro-osteogenic, pro-structural, and functionally regenerative phenotype.

# 3. Conclusion

In summary, we developed a multifunctional GaMOF–$Cu_2O$–integrated GelMA hydrogel that simultaneously targets bacterial eradication, immunomodulation, and tissue regeneration. Through a combination of physicochemical characterization, antibacterial assays, immunoregulatory evaluations, osteogenic differentiation studies, *in vivo* infection models, and transcriptomic profiling, our findings collectively demonstrate the therapeutic potential of this dual-metal hydrogel platform. The incorporated $Ga^{3+}$ disrupts bacterial iron metabolism while $Cu^{+}$ catalyzes ROS generation, producing a synergistic antibacterial effect capable of eliminating both planktonic and biofilm-embedded pathogens. Beyond bactericidal activity, GelMA@GaCu effectively reprograms macrophage polarization toward a pro-regenerative M2 phenotype, attenuates inflammatory signaling, and enhances osteogenic activation in BMSCs, thereby creating a favorable microenvironment for tissue repair. *In vivo*, GelMA@GaCu accelerated wound closure, reduced inflammatory infiltration, and promoted collagen deposition in infected tissues, confirming its ability to simultaneously control infection and support structural regeneration.

Taken together, this work introduces a new class of multifunctional hydrogel-based therapeutics that integrates antibacterial potency with immune regulation and regenerative enhancement. By combining Ga/Cu-mediated biochemical mechanisms with the structural and delivery advantages of GelMA, GelMA@GaCu represents a promising strategy for treating refractory bone and soft tissue infections, particularly those complicated by multidrug resistance and biofilm formation. This platform provides a foundation for future translational development of intelligent biomaterials aimed at addressing the dual challenges of infection control and tissue reconstruction.

# 4. Experimental section

## 4.1 Preparation of GelMA precursor

GelMA powder was dissolved in deionized water at 50 °C to obtain a 10 wt% transparent solution. LAP photoinitiator was dissolved separately (0.25 wt%) and added to the GelMA solution under gentle stirring until fully mixed.

## 4.2 Incorporation of Ga and Cu ions

To prepare Ga/Cu-loaded hydrogels, $Ga(NO_3)_3$ solution (10 mg $mL^{-1}$) and $Cu_2O$ nanoparticles (1 mg $mL^{-1}$) were added dropwise into the GelMA precursor under constant stirring. The total concentration of $Ga^{3+}$ and $Cu^{+}$ in the final hydrogel was controlled by varying the added volumes (typically 100–300 μg of each metal per mL precursor). The mixture was stirred for 10 min to allow initial ion–polymer coordination. Subsequently, the solution was poured into molds (diameter: 6 mm; thickness: 1 mm).

## 4.3 Photopolymerization

The precursor solution was irradiated under 405 nm LED light (intensity: 30 mW $cm^{-2}$) for 60 s to complete crosslinking and yield the GelMA@GaCu hydrogel, which was then washed thoroughly with ultrapure water to remove unbound ions and stored at 4 °C.

## 4.4 TEM imaging

Hydrogel samples were freeze-dried, ground gently, and dispersed in ethanol by ultrasonication prior to TEM imaging (JEM-2100F, JEOL). The acceleration voltage was set at 200 kV. High-resolution TEM (HRTEM) and EDS mapping were used to confirm Ga/Cu distribution.

## 4.5 Dynamic light scattering and zeta potential

Particle distributions were measured using a Zetasizer Nano ZS (Malvern Instruments). Samples were diluted to 0.2 mg $mL^{-1}$ prior to testing. Zeta potential was evaluated using folded capillary cells.

## 4.6 ICP-OES analysis

To quantify the actual Ga loading, hydrogels were fully degraded with 1% (v/v) $HNO_3$ and analyzed using ICP-OES (Agilent 5110). Calibration curves (0–10 ppm) were prepared freshly using Ga standard solutions.

## 4.7 pH-Responsive Ga ion release

GelMA@GaCu hydrogels (diameter 10 mm) were immersed in 10 mL of PBS (pH 7.4) or MES buffer (pH 6.0) at 37 °C with gentle shaking (100 rpm). At predetermined time points (2, 8, 16, 24, 48 h), 1 mL supernatant was collected and replaced with fresh buffer. The $Ga^{3+}$ content was quantified *via* ICP-OES. The cumulative release percentage was calculated as: release rate = $M_0/M_t \times 100\%$, where $M_0$ is the initial Ga amount in the hydrogel.

## 4.8 Antibacterial activity evaluation

MRSA and *E. coli* cultures were adjusted to $OD_{600}$ = 0.01, then incubated with GelMA@GaCu (1–100 ppm), $Ga^{3+}$, $Cu^{+}$, or pure GelMA for 12 h at 37 °C. After treatment, bacterial suspensions were serially diluted ($10^{-1}$ to $10^{-5}$) and plated onto LB agar plates. Colonies were counted after 24 h incubation. DCFH-DA (1 μM) was added to bacterial suspensions treated with GelMA@GaCu for 2 h. ROS levels were determined using a fluorescence microplate reader ($E_x/E_m$ = 488/520 nm). MRSA cells were stained with $DiBAC_4(3)$ (8 μM), incubated 15 min, and analyzed by flow cytometry (Guava easyCyte6-2L). Bacterial cells were fixed with 3% formaldehyde, dehydrated through ascending ethanol series, freeze-dried, and imaged by TEM.

### 4.9 Transcriptomic sequencing and bioinformatics

After 24 h incubation with GelMA@GaCu extract, total RNA was extracted using TRIzol reagent. RNA purity and concentration were determined using NanoDrop 2000. Sequencing libraries were prepared using NEBNext Ultra II RNA Library Prep Kit and sequenced on an Illumina NovaSeq platform (150 bp paired-end).

### 4.10 In vivo wound healing model

A full-thickness circular wound (6 mm) was created on the dorsal skin of mice under anesthesia. MRSA ($1 \times 10^8$ CFU $mL^{-1}$, 100 μL) was applied onto each wound. Mice were randomized into 5 groups ($n$ = 5 per group):PBS, GelMA, Ga/Cu ions, GelMA@Ga, and GelMA@GaCu. Treatments (100 μL) were applied daily. Wounds were photographed on days 1 and 7. Healing area was quantified using ImageJ. Wound tissues were harvested for H&E staining, CFU quantification, and cytokine analysis.

### 4.11 Cytokine analysis

Wound tissues were homogenized in cold PBS and centrifuged at 8000 rpm for 10 min. IL-6 and TNF-α levels in supernatants were measured using ELISA kits (Jianglaibio) following the manufacturer's instructions.

### 4.12 Statistical analysis

All experiments were performed in triplicate unless otherwise noted. Data were reported as mean ± SD. Statistical significance was assessed using one-way ANOVA with Tukey's *post hoc* test ($P < 0.05$).

## Conflicts of interest

The authors declare no competing financial interest.

## Data availability

All data generated or analysed during this study are included in this published article and its supplementary information (SI). Supplementary information is available. See DOI: https://doi.org/10.1039/d5ma01501d.

## Acknowledgements

Hai Zhu contributed to this work alone. This study was supported by Natural Science Research Cultivation Program of Northern Jiangsu Institute of Clinical Medicine, Nanjing Medical University (SLKYMS20240109) and Basic Research Program of Huai'an Science and Technology Plan Projects (HAB2024008). All the animal procedures were performed under the protocols approved by Animal Welfare Ethics Committee of The Affiliated Huaian No. 1 People's Hospital (KY-2022-111-01).

## References

1 X. Shu, *et al.*, Transcription tuned by S-nitrosylation underlies a mechanism for Staphylococcus aureus to circumvent vancomycin killing, *Nat. Commun.*, 2023, **14**(1), 2318.
2 D. G. Mediati, *et al.*, RNase III-CLASH of multi-drug resistant Staphylococcus aureus reveals a regulatory mRNA 3'UTR required for intermediate vancomycin resistance, *Nat. Commun.*, 2022, **13**(1), 3558.
3 S. H. Bengtson, *et al.*, Kinin receptor expression during Staphylococcus aureus infection, *Blood*, 2006, **108**(6), 2055–2063.
4 R. P. Vonberg, *et al.*, Impact of the suctioning system (open vs. closed) on the incidence of ventilation-associated pneumonia: Meta-analysis of randomized controlled trials, *Intensive Care Med.*, 2006, **32**(9), 1329–1335.
5 S. J. Joseph and T. D. Read, Bacterial population genomics and infectious disease diagnostics, *Trends Biotechnol.*, 2010, **28**(12), 611–618.
6 A. M. Edwards, *et al.*, Staphylococcus aureus keratinocyte invasion is dependent upon multiple high-affinity fibronectin-binding repeats within FnBPA, *PLoS One*, 2011, **6**(4), e18899.
7 P. Fratzl, Imaging techniques: Extra dimension for bone analysis, *Nature*, 2015, **527**(7578), 308–309.
8 R. Wu, *et al.*, A Heterocatalytic Metal-Organic Framework to Stimulate Dispersal and Macrophage Combat with Infectious Biofilms, *ACS Nano*, 2023, **17**(3), 2328–2340.
9 A. A. Ahmed, *et al.*, Preparation and characterization of antibacterial $P_2O5$-CaO-$Na_2O$-$Ag_2O$ glasses, *J. Biomed. Mater. Res., Part A*, 2011, **98**(1), 132–142.
10 S. Yamaguchi, *et al.*, Two-in-One Biointerfaces-Antimicrobial and Bioactive Nanoporous Gallium Titanate Layers for Titanium Implants, *Nanomaterials*, 2017, **7**(8), 229.
11 F. Li, *et al.*, Advancement of Gallium and Gallium-Based Compounds as Antimicrobial Agents, *Front. Bioeng. Biotechnol.*, 2022, **10**, 827960.
12 C. Zhu, *et al.*, High-Antimicrobial Gallium-Doped Zinc Oxide Thin Films on Bio-Based Poly(Ethylene Furanoate) Substrates for Food Packaging Application, *Membranes*, 2023, **13**(2), 239.
13 S. K. Ramadass, *et al.*, Type I collagen peptides and nitric oxide releasing electrospun silk fibroin scaffold: A multifunctional approach for the treatment of ischemic chronic wounds, *Colloids Surf., B*, 2019, **175**, 636–643.
14 S. Lin, *et al.*, Porous Iron-Carboxylate Metal-Organic Framework: A Novel Bioplatform with Sustained Antibacterial Efficacy and Nontoxicity, *ACS Appl. Mater. Interfaces*, 2017, **9**(22), 19248–19257.
15 N. Song, *et al.*, Supramolecular nanotheranostics based on pillarenes, *Theranostics*, 2019, **9**(11), 3075–3093.
16 Y. Wang, *et al.*, Metal-organic frameworks for stimuli-responsive drug delivery, *Biomaterials*, 2020, **230**, 119619.
17 G. Wyszogrodzka-Gaweł, *et al.*, An Inhalable Theranostic System for Local Tuberculosis Treatment Containing an Isoniazid Loaded Metal Organic Framework Fe-MIL-101-NH2-From Raw MOF to Drug Delivery System, *Pharmaceutics*, 2019, **11**(12), 687.

18 Z. Zhang, *et al.*, A Review on Metal-Organic Framework-Derived Porous Carbon-Based Novel Microwave Absorption Materials, *Nano-Micro Lett.*, 2021, **13**(1), 56.
19 G. Skorupskii, *et al.*, Electrical conductivity through π–π stacking in a two-dimensional porous gallium catecholate metal-organic framework, *Ann. N. Y. Acad. Sci.*, 2022, **1518**(1), 226–230.
20 Y. Liu, *et al.*, Directional Freeze-Casting Cryogel Loaded with Quaternized Chitosan Modified Gallium Metal-Organic Frameworks to Capture and Eradicate the Resistant Bacteria for Guided Regeneration in Infected Bone Defects, *Adv. Mater.*, 2025, e2414437.
21 J. T. Seil and T. J. Webster, Antimicrobial applications of nanotechnology: methods and literature, *Int. J. Nanomed.*, 2012, **7**, 2767–2781.
22 M. Haeili, *et al.*, Copper complexation screen reveals compounds with potent antibiotic properties against methicillin-resistant Staphylococcus aureus, *Antimicrob. Agents Chemother.*, 2014, **58**(7), 3727–3736.
23 J. S. Möhler, *et al.*, Silver bullets: A new lustre on an old antimicrobial agent, *Biotechnol. Adv.*, 2018, **36**(5), 1391–1411.
24 P. Mahmoudi, *et al.*, Antibacterial Ti-Cu implants: A critical review on mechanisms of action, *Mater. Today Bio*, 2022, **17**, 100447.
25 A. Hou, *et al.*, UV Light-Induced Generation of Reactive Oxygen Species and Antimicrobial Properties of Cellulose Fabric Modified by 3,3',4,4'-Benzophenone Tetracarboxylic Acid, *ACS Appl. Mater. Interfaces*, 2015, **7**(50), 27918–27924.
26 F. C. Morris, *et al.*, The Mechanisms of Disease Caused by Acinetobacter baumannii, *Front. Microbiol.*, 2019, **10**, 1601.
27 H. N. Abdelhamid and A. P. Mathew, Cellulose-Based Nanomaterials Advance Biomedicine: A Review, *Int. J. Mol. Sci.*, 2022, **23**(10), 5405.
28 P. Sammanee, *et al.*, Decontamination of Pathogenic and Spoilage Bacteria on Pork and Chicken Meat by Liquid Plasma Immersion, *Foods*, 2022, **11**(12), 1743.
29 H. L. Rutledge and F. A. Tezcan, Electron Transfer in Nitrogenase, *Chem. Rev.*, 2020, **120**(12), 5158–5193.
30 R. Jenjob, T. Phakkeeree and D. Crespy, Core-shell particles for drug-delivery, bioimaging, sensing, and tissue engineering, *Biomater. Sci.*, 2020, **8**(10), 2756–2770.
31 B. J. O'Grady, *et al.*, Development of an N-Cadherin Biofunctionalized Hydrogel to Support the Formation of Synaptically Connected Neural Networks, *ACS Biomater. Sci. Eng.*, 2020, **6**(10), 5811–5822.
32 F. Wei, *et al.*, Host Response to Biomaterials for Cartilage Tissue Engineering: Key to Remodeling, *Front. Bioeng. Biotechnol.*, 2021, **9**, 664592.
33 B. Velasco-Rodriguez, *et al.*, Hybrid Methacrylated Gelatin and Hyaluronic Acid Hydrogel Scaffolds. Preparation and Systematic Characterization for Prospective Tissue Engineering Applications, *Int. J. Mol. Sci.*, 2021, **22**(13), 6758.
34 K. Sun, *et al.*, Injectable BMP-2 gene-activated scaffold for the repair of cranial bone defect in mice, *Stem Cells Transl. Med.*, 2020, **9**(12), 1631–1642.
35 H. Kang, *et al.*, Magnetic Manipulation of Reversible Nanocaging Controls In Vivo Adhesion and Polarization of Macrophages, *ACS Nano*, 2018, **12**(6), 5978–5994.
36 M. Ivec, *et al.*, Interactions of macrophages with probiotic bacteria lead to increased antiviral response against vesicular stomatitis virus, *Antiviral Res.*, 2007, **75**(3), 266–274.
37 T. H. M. Pham, *et al.*, Salmonella-Driven Polarization of Granuloma Macrophages Antagonizes TNF-Mediated Pathogen Restriction during Persistent Infection, *Cell Host Microbe*, 2020, **27**(1), 54–67.e5.
38 R. Feng, *et al.*, Knowledge gaps in immune response and immunotherapy involving nanomaterials: Databases and artificial intelligence for material design, *Biomaterials*, 2021, **266**, 120469.
39 L. Zhao, *et al.*, Natural Killer Cells Regulate Pulmonary Macrophages Polarization in Host Defense Against Chlamydial Respiratory Infection, *Front. Cell. Infect. Microbiol.*, 2021, **11**, 775663.
40 W. Wang, *et al.*, SPP1 and CXCL9 Promote Non-alcoholic Steatohepatitis Progression Based on Bioinformatics Analysis and Experimental Studies, *Front. Med.*, 2022, **9**, 862278.
41 Z. Liu, *et al.*, Ion channel gene GJB2 influences the intercellular communication by Up-regulating the SPP1 signaling pathway identified by the single-cell RNA sequencing in lung adenocarcinoma, *Front. Oncol.*, 2023, **13**, 1146976.